ARTICLE IN PRESS

Nature Communications

https://doi.org/10.1038/s41467-026-72731-y

Article in Press

Atomic dynamics of solid-gas interfaces unveil dual-layer formation and WS_2 nucleation driven by multistep phase-transition

Received: 23 July 2025

Accepted: 21 April 2026

[redacted]

Qinwei An, Xueyang Zhang, Yuanlin Fang, Wen Zhao, Wenqi Xiong, Feng Li, Shengjun Yuan & Jie Wang

Cite this article as: An, Q., Zhang, X., Fang, Y. *et al.* Atomic dynamics of solid-gas interfaces unveil dual-layer formation and WS_2 nucleation driven by multistep phase-transition. *Nat Commun* (2026). https://doi.org/10.1038/s41467-026-72731-y

We are providing an unedited version of this manuscript to give early access to its findings. Before final publication, the manuscript will undergo further editing. Please note there may be errors present which affect the content, and all legal disclaimers apply.

If this paper is publishing under a Transparent Peer Review model then Peer Review reports will publish with the final article.

ARTICLE IN PRESS

© The Author(s) 2026. **Open Access** This article is licensed under a Creative Commons Attribution-NonCommercial-NoDerivatives 4.0 International License, which permits any non-commercial use, sharing, distribution and reproduction in any medium or format, as long as you give appropriate credit to the original author(s) and the source, provide a link to the Creative Commons licence, and indicate if you modified the licensed material. You do not have permission under this licence to share adapted material derived from this article or parts of it. The images or other third party material in this article are included in the article's Creative Commons licence, unless indicated otherwise in a credit line to the material. If material is not included in the article's Creative Commons licence and your intended use is not permitted by statutory regulation or exceeds the permitted use, you will need to obtain permission directly from the copyright holder. To view a copy of this licence, visit http://creativecommons.org/licenses/by-nc-nd/4.0/.

Atomic dynamics of solid-gas interfaces unveil dual-layer formation and WS_2 nucleation driven by multistep phase-transition

Qinwei An[1,2]*, Xueyang Zhang[1,2], Yuanlin Fang[3], Wen Zhao[3]*, Wenqi Xiong[4], Feng Li[1,2], Shengjun Yuan[5,6], Jie Wang[7]

[1]Shaanxi Key Laboratory of Optical Information Technology and School of Physical Science and Technology, Northwestern Polytechnical University, Xi'an, China.

[2]Key Laboratory of Light Field Manipulation and Information Acquisition, Ministry of Industry and Information Technology, Northwestern Polytechnical University, Xi'an, China.

[3]Shandong Key Laboratory of Intelligent Energy Materials, School of Materials Science and Engineering, China University of Petroleum (East China), Qingdao, China.

[4]Institute of Quantum Materials and Physics, Henan Academy of Sciences, Zhengzhou, China.

[5]Key Laboratory of Artificial Micro- and Nano-structures of Ministry of Education and School of Physics and Technology, Wuhan University, Wuhan, China.

[6]Wuhan Institute of Quantum Technology, Wuhan, China.

[7]Analytical & Testing Center, Northwestern Polytechnical University, Xi'an, China.

*Qinwei An, Wen Zhao. Email: anqw@nwpu.edu.cn; zhaowen@upc.edu.cn

Atomic-scale solid–gas interface (SGI) dynamics remain elusive due to transient intermediates, complex interfacial environments, and challenges of real-time characterization. Using an environmental transmission electron microscopy cell as a microreaction chamber combined with atomic-resolution in-situ imaging, here we directly visualize SGI reactions at the interface of transition metal oxidate $WO_{2.72}$ nanowire under reactive gas environments. We reveal that initial SGI interactions trigger surface restructuring into a dual-layer configuration, consisting of an uppermost amorphous layer and an underlying lattice-distorted condensed region. The amorphous surface layer acts as a quasi-liquid precursor reservoir that promotes reversible crystalline–amorphous transformations and short-range ordering for critical nucleus formation, while the roughened, defect-rich subsurface interface provides energetically favorable sites for WS_2 nucleation and vertical growth. Furthermore, in-situ atomic-scale observations of MoS_2 nucleation and growth via SGI reactions demonstrate the generality of this mechanism. The atomistic processes governing interfacial reconstruction and nucleation are further corroborated by theoretical calculations. Our results establish a dual-layer-mediated reconstruction pathway during SGI reactions, overturning the conventional view of atomically sharp and static reaction fronts. Moreover, these findings provide insights into multistep phase-transition-governed WS_2 nucleation and growth, enabling controlled synthesis of 2D WS_2 and MoS_2 toward atomic-scale manufacturing.

Introduction

Solid–gas interface (SGI) reactions are ubiquitous across geochemical, planetary, and industrial systems, from early solar condensation to catalytic conversion and materials synthesis[1-18]. These reactions dictate pathways, efficiencies, and selectivity in catalysis[3-6], energy conversion[7, 8], gas sensing[9, 10], corrosion[11, 12], and functional materials synthesis[13-18]. Extensive studies have investigated factors influencing SGI reactions, such as temperature, pressure, gas composition, surface morphology, and material composition[19]. Based on these findings, fundamental reaction models—including the shrinking core model, the continuous model, and the grain model—were established[20, 21]. While classical models (e.g., shrinking core model) describe macroscale kinetics, atomic-scale dynamics remain unresolved due to transient intermediates, complex interfacial environments, and limitations in real-time characterization.

Recently, interaction involving metal nanoparticles and metal-oxide supports have been conducted using in-situ transmission electron microscopy (TEM)[22-25]. These in-situ observations have uncovered phenomena such as the reconstruction of TiO_2 overlayers on metal nanoparticles, the dynamic rotation of Au-TiO_2 system under varying redox conditions (O_2, H_2, H_2/O_2, CO/O_2), twin-protrusion features of adsorbed water on TiO_2 (001) surfaces[4], and gas–solid redox reaction dynamics between gas (CO and H_2) and NiO[25], as summarized in Supplementary Table 1. Yet, the atomic-scale underlying mechanisms governing SGI dynamics, including atomic-scale solid surface reconstruction, nucleation, growth and phase transition dynamics during dynamic SGI reaction, and the functional role of different transient phases—remain unresolved. Critical gaps persist in probing: (i) real-time atomistic lattice rearrangement at initial stage of SGI reactions, (ii) the roles of reconstructed solid layers during following SGI reaction, and (iii) the nucleation, growth and phase transition dynamics for diverse nuclei during the SGI reactions. These challenges demand atomic-resolution imaging of dynamic SGI reactions under operando conditions, coupled with precise control of reaction kinetics—a capability beyond current methodologies.

Transition metal dichalcogenide (TMDC) nanotubes (NTs), particularly those based on WS_2 and MoS_2, have been synthesized via the so-called "surface-inward" mechanism[26-30]. In this process, oxygen-deficient transition metal oxide nanowires, such as $WO_{2.72}$ and MoO_2 nanowires, serve as the dominant precursor phases and nucleation templates for TMDC formation. These nanowires are first generated through the high-temperature sulfidation of transition metal oxides (WO_3 or MoO_3). Subsequently, reaction with H_2S/S vapor and H_2 induces conversion of the oxide nanowhiskers into TMDC nanotubes, driven by a Kirkendall-type diffusion process[27, 30]. More recently, an in-situ SEM microreactor with H_2 and H_2S sources enabled direct observation of the growth process, displaying a dynamic reaction mechanism termed the receding oxide core[31], which complements the classical surface-inward model and has been kinetically evaluated. These findings demonstrate that these reaction systems provide a platform for in-situ investigation of dynamic SGI reaction.

In this work, we employ oxygen deficient transition metal oxidate nanowires ($WO_{2.72}$ and MoO_2) as model solid precursors. Their high surface-to-volume ratio and abundance of low-coordination sites facilitate SGI reactions at relatively low temperatures (≈ 200-300 °C), with reaction kinetics tunable via the sulfur vapor supply. Moreover, their well-defined crystallographic order enables atomic-scale tracking of structural evolution during SGI processes. To overcome the above limitations for atomic-resolution imaging of dynamic SGI reactions, we utilize an operando ETEM cell as a microreaction chamber, enabling atomic-resolution imaging of dynamic SGI reactions under realistic chemical vapor deposition (CVD) conditions. This approach allows direct visualization of TMDC nucleation at the interface of oxygen-deficient oxide nanowires in real time. We find that initial gas adsorption triggers a dual-layer reconfiguration consisting of surface amorphization and subsurface lattice distortion. This interfacial restructuring mediates subsequent phase transformation: the amorphous surface layer functions as a mobile precursor reservoir that promotes rapid cluster assembly, while the underlying roughened subsurface—characterized by atomic steps, vacancies, and lattice mismatch—serves as a template for nucleation and growth. These findings reveal that SGI reactions are not merely passive consumption processes, but active nano-engineering phenomena in which interfacial reconstruction directs phase evolution, challenging conventional static reaction-front paradigms[2, 21].

Results

In-situ observation of solid-gas interface reactions

Gas-solid reactions in conventional chemical vapor reaction process—for example the synthesis of $WO_{2.72}/WS_2$ core/shell nanotube—are typically carried out far from equilibrium, often under high temperatures or pressures. Such conditions lead to rapid and poorly controlled reaction kinetics, making it difficult to probe the dynamic evolution of the system. As a result, only the initial and final states can usually be characterized, while the intermediate processes remain largely inaccessible and effectively a “black box.” In this work, we deliberately reduced the reaction temperature to 200-300 °C to slow the reaction kinetics. In addition, sulfur grains were used as a controllable sulfur vapor source, enabling precise modulation of the reduction rate through adjustment of sulfur quantity. These strategies effectively decelerate the SGI dynamics, allowing us to capture atomic-scale structural evolution with millisecond temporal resolution.

We performed operando studies of solid-gas interfacial reaction dynamics using oxygen-deficient $WO_{2.72}$ nanowires as model precursor in a closed cell environmental TEM micro-reaction (Fig. 1a). The system integrates an electron-transparent Si_3N_4 window, gas inlet/outlet ports, and a ceramic heater (Supplementary Fig. 1). The electron-transparent windows of microchamber enabled direct visualization of dynamic structural evolution at SGI. The chip was capable of heating up to 980 °C at a controlled ramping rate of $0.5°C\ s^{-1}$. Operando TEM movies were acquired at an accelerating voltage of 200 kV with a beam dose rate of $7\times10^4\ e^-\ nm^{-2}\ s^{-1}$, a temporal resolution of 500 ms per frame, and an image size of 2048 × 2048 pixels. Pre-synthesized $WO_{2.72}$ nanowires (Supplementary Fig. 2, Methods) were transferred to the window, with sulfur grains serving as the chalcogen source and a H_2/Ar (5%/95%) mixture acting as the reductant. The amount of sulfur loaded in the cell enabled precise control of sulfur vapor pressure, thereby regulating the kinetics of the SGI reaction.

Fig. 1b shows a representative in-situ TEM frame of the pre-synthesized pristine $WO_{2.72}$ crystals on the Si_3N_4 electron-transparent window. Prior to heating, the nanowires exhibited well-defined (010) and (103) lattice planes (0.37 and 0.38 nm spacings) along the [−301] zone axis, confirming high crystallinity (Fig. 1c). However, room-temperature electron irradiation induced noticeable carbon deposition on the nanowire surface, which was effectively removed by mild annealing at 200 °C (Fig. 1d). Upon heating to ≈ 50 °C, sulfur grains have completely evaporated (Supplementary Fig. 3). When the temperature exceeded 200 °C, intensified sulfur evaporation and rapid oxygen consumption triggered pronounced surface reconstruction (Supplementary Fig. 4). The initial SGI reaction produced a distinct three-region structure: an uppermost amorphous layer, a subsurface distortion layer with displaced and condensed lattice planes, and a pristine crystalline core. These regions were separated by sharp interfaces, indicating rapid and spatially confined structural transformation. These surface restructures represent the early stages of SGI reaction, and as the reactions continued, operando imaging further reveals that this interfacial restructuring mediates subsequent phase transformation: the amorphous surface layer functions as a mobile precursor reservoir that promotes rapid cluster assembly, while the underlying roughened subsurface—characterized by atomic steps, vacancies, and lattice mismatch—serves as a template for nucleation and growth.

Zoom-in TEM frame at 21 min 56 s captures the emergence of a new nanocrystal at the amorphous–distorted interface (Fig. 1e, d). This nucleus exhibits an interplanar spacing of 0.380 nm, consistent with the (001) planes of metastable orthorhombic $WO_{2.66}$. This observation confirms progressive oxygen depletion driven by continuous reduction within the surface quasi-liquid interphase (Supplementary Note 1, Supplementary Figs. 5, 6). As the reduction proceeds, the $WO_{2.66}$ phase gradually disappears. At 34 min 34 s (Fig. 1e,f), multilayered nanocrystals with a characteristic spacing of 0.622 nm—matching the *c*-axis spacing of hexagonal WS_2—are observed at the same interface. These WS_2 nuclei originate at the strained subsurface and grow vertically from the nanowire surface, in contrast to the lateral growth typically seen on planar substrates. As growth proceeds, propagation follows the nanowire curvature, initiating rolling behavior characteristic of nanotube formation[31]. These observations demonstrate that, rather than acting as a passive reaction front, the dynamically reconfigured dual-layer interface actively regulates precursor supply, strain distribution, and crystallographic alignment, thereby dictating nucleation geometry and subsequent phase evolution, providing a detailed physical picture of the SGI reaction at the atomic scale.

Atomic dynamics of dual-layer formation during SGI reaction

To elucidate the atomic dynamics of SGI during the reaction, we selected a representative region, highlighted by the white rectangle in Fig. 2a. Situated at the boundary between the distorted subsurface layer and the underlying pristine lattice, this region initially exhibits a well-ordered lattice configuration at 3 min 4 s in the zoomed-in in-situ images. Within seconds of H_2/S exposure, however, the lattice underwent rapid decomposition. Oxygen deficiency due to the SGI reactions triggers bond rupture (3 min 4.5 s), induces W-O-W angle rotation (3 min 9 s), and ejects atom/W_xO_y cluster (3 min 13-15 s). Ultimately, it replaces pristine lattice fringes with a vacancy-rich distorted phase (Fig. 2b, Supplementary Movie 1). These coupled bond-breaking and bond-rotation events progressively destabilize the local coordination environment, transforming the initially crystalline surface into a disordered region with a roughened interface (Fig. 2b, white lines; Supplementary Fig. 7). This series of atomic-scale restructuring processes—including bond dissociation, angular reorientation, and atom extraction—illustrates how reduction-induced oxygen depletion drives lattice destabilization and interfacial roughening, summarized and schematically illustrated in Fig. 2c.

Notably, the restructuring is not confined to the outermost surface. Vacancy formation and bond destabilization facilitate inward propagation of disorder, driving progressive subsurface reconstruction. Consequently, the nanowire becomes stratified into three distinct regions: (a) an amorphous surface layer, (b) a distorted subsurface lattice, and (c) an intact crystalline core (Fig. 2d). As the SGI reaction proceeds, time-resolved in-situ TEM imaging captures the continuous evolution of this dual-layer architecture (Supplementary Movie 2). The distorted subsurface region gradually thickens, reflecting sustained oxygen extraction and lattice reorganization that advance from the surface toward the nanowire interior. These real-space observations are further corroborated by fast Fourier transform (FFT) analysis (Fig. 2d, insets). In the surface region, diffuse scattering and progressive elongation of the (103) Bragg reflections are significantly more pronounced than in the interior, indicating enhanced lattice distortion and structural divergence induced by SGI-driven rearrangement. To quantify this evolution, we tracked the interplanar spacing of the (103) planes in both surface and interior regions over time (Fig. 2e) and measured the thickness of the distorted layer (Fig. 2f). These parameters were extracted from time-resolved TEM frames and their corresponding FFT reflections, enabling a quantitative description of the dynamic interfacial reconstruction. The results reveal progressive inward propagation of structural distortion during SGI conversion, ultimately transforming the near-surface region into a fully distorted layer capped by a surface quasi-liquid phase. This distorted lattice layer acts as a kinetic intermediary that facilitates phase transformation through effective strain accommodation, defect propagation, and localized chemical reorganization. Meanwhile, the overlying amorphous surface layer behaves as a quasi-liquid interphase, serving as a dynamic precursor reservoir that sustains continued SGI reactions. A similar quasi-liquid intermediate enabling mass transport has been reported at solid–liquid interfaces, where it mediates material transfer between metal nanoparticles and the surrounding liquid[32].

Complementing the operando observations, our CVD system enables rapid cooling to ambient temperature, instantly ‘freezing’ the products at intermediate stage during SGI for ex-situ characterization. HRTEM and STEM of a representative specimen reacted at 800 °C reveals a well-preserved trilayer architecture consisting of an amorphous surface layer, a distorted subsurface lattice, and an intact pristine core, separated by sharp interfaces (Supplementary Figs. 8-13). FFT patterns and corresponding lattice-fringe intensity profiles clearly distinguish the crystallographic signatures of these regions, with pronounced peak broadening and anisotropic distortion in the subsurface lattice. These features are fully consistent with the lattice reconstruction dynamics captured under operando conditions, providing independent validation of the dual-layer evolution mechanism. To disentangle intrinsic lattice reconstruction from potential electron-beam–induced artifacts during the SGI reaction, we performed a comprehensive set of control experiments. These include ex-situ structural characterization of reacted $WO_{2.72}$ crystals prepared without electron-beam exposure, systematic comparisons under different electron dose rates, and beam-blanking experiments during in-situ observation. All control measurements consistently demonstrate that the lattice reconstruction and dual-layer formation observed in this study are intrinsic mechanism governing the SGI reaction (Supplementary Note 2, Supplementary Figs. 14-16). Although electron irradiation can accelerate the rearrangement kinetics, it does not dictate the structural evolution associated with dual-layer formation. We therefore conclude that the observed lattice construction and dual-layer formation are primarily governed by the intrinsic thermodynamics and chemical driving forces of the SGI reaction, rather than by electron-beam effects.

Dual-layer-mediated WS_2 nucleation at SGI

The amorphous layer and the sub-surface distorted interlayer formed during initial solid-gas reactions significantly modified the SGI. Their roles in subsequent SGI reaction are required to be elucidated. As the SGI reactions progress, new crystallization phases nucleate at the modified interface. Figure 3a, b show the nucleation dynamics of two distinct crystalline phases, revealing that the nuclei form primarily within the uppermost amorphous layer and preferentially anchor to the rough interface of the subsurface distorted interlayer, as indicated by arrows in the images. The amorphous layer acts as a precursor reservoir, enhancing atomic mobility and bond reconfiguration frequency, thus facilitating the assembly of short-range ordered units and promoting critical nucleus formation. Density functional theory (DFT) calculations suggest that nucleation on $WO_{2.72}$ is more stable at the SGI with oxygen-terminated vacancies or defects (0.09 eV $Å^{-2}$) compared to the pristine lattice interface (0.08 eV $Å^{-2}$) (Supplementary Fig. 17). Therefore, the rough interface—characterized by atomic steps, vacancies, and lattice mismatch—provides energetically favorable attachment sites, contrasting with defect-free surfaces. The amorphous precursor reservoir and the distorted subsurface layer form a synergistic system that triggers the nucleation of new crystalline phases.

Further structural analysis reveals distinct nucleation pathways for two crystalline phases. At 3 min 52 s, medium-range ordering emerges at the amorphous–distorted lattice interface (Fig. 3a, Supplementary Movie 3), with an interlayer spacing of 0.383 ± 0.02 nm. This value is most consistent with the (001) planes of orthorhombic $WO_{2.66}$, suggesting that the satellite nucleus may originate from a reduced intermediate phase (Supplementary Note 3.1, Supplementary Fig. 18). This observation aligns with the phase diagram and computed energy landscape of the W–S–O system (Fig. 3c), which predict the stabilization of oxygen-deficient tungsten oxides prior to full sulfurization[33]. These findings demonstrate that SGI reactions proceed through a stepwise reduction–sulfurization pathway rather than a direct oxide-to-sulfide transformation. The formation of metastable $WO_{2.66}$ signals progressive oxygen extraction and structural rearrangement within the uppermost amorphous layer, where a high concentration of mobile $WO_{2.72-x}$ units is generated. These undercoordinated tungsten–oxygen species, released by reduction-induced bond cleavage, exhibit enhanced diffusivity and chemical reactivity, facilitating short-range ordering and cluster assembly. This reorganization lowers the kinetic barrier for intermediate-phase nucleation, stabilizing the transient $WO_{2.66}$ phase. This $WO_{2.66}$ nuclei expand to ≈ 4 nm within 8 s (4 min 0 s, Fig. 3a and Supplementary Fig. 19), but later degenerates upon reaction with H/S species, reverting to disordered clusters (Supplementary Fig. 20 and Supplementary Movie 3). After re-incubation, the $WO_{2.66}$ (001) plane reforms (4 min 15.5 s, Supplementary Fig. 21), only to disorder again due to drastic atoms absorption and desorption at the surface (4 min 27s, Supplementary Fig. 21). This reversible order-disorder transitions, reminiscent of dynamics observed in Au crystal[34] and copper-catalyzed CO_2 electroreduction reactions[32], recurs throughout the SGI reaction (Supplementary Fig. 22), with oscillation periods progressively shortening until stabilization as disordered clusters, driven by continuous oxygen depletion and sulfur incorporation (Supplementary Fig. 23). Moreover, nucleation of numerous orthorhombic $WO_{2.66}$ domains with identical interlayer spacing has been identified on the Si_3N_4 window (Supplementary Fig. 24), further supporting the role of the orthorhombic $WO_{2.66}$ phase as a critical intermediate in the reduction of $WO_{2.72-x}$ vapor through reaction with H_2/S species.

At 21 min 17 s, a second, distinct nucleation event is observed, accompanied by reversible order–disorder transitions (Supplementary Figs. 25, 26, Supplementary Movie 4). In contrast to the $WO_{2.66}$ intermediate, this phase exhibits (1) a higher transition frequency during its early evolution and (2) eventual stabilization into a persistent nucleus at 22 min 30 s, despite continued H_2/S exposure. During nucleation, an initial structure with an interplanar spacing of 0.268 nm emerges and progressively transforms into a multilayered configuration with a spacing of 0.622 nm. The latter matches the (002) interlayer distance of hexagonal WS_2, confirming the formation of a layered crystallite at the SGI. Notably, the WS_2 layers stack along the (002) direction, oriented perpendicular to the $WO_{2.72}$ nanowire surface, indicative of vertical growth rather than lateral expansion. According to the crystallographic matching, dynamic fluctuation signature, thermodynamic consistency with the computed energy landscape (Fig. 3c, Supplementary Fig. 27), the transient structure with 0.268 nm spacing prior to multilayer formation can be assigned to a trigonal WS_2 nanocrystal oriented along the (012) direction (Supplementary Note 3.2, Supplementary Fig. 28). This structural evolution indicates a polymorphic transition from a metastable trigonal nucleus to the thermodynamically favored hexagonal multilayered phase, consistent with the above experimentally reported structural phase transitions. Furthermore, these mechanistic insights are further supported by similar nucleation sequence of WS_2 on Si_3N_4 window **(**Supplementary Figs. 29, 30**)** and following simulations of lattice reconstruction and nucleation at the SGI, which reproduce the experimentally observed structural evolution.

Complementary to operando imaging, ex-situ comparative analysis of pristine $WO_{2.72}$ crystal, the final $WO_{2.72}/WS_2$ core/shell structure, 2H WS_2 multilayer, and two transient states (intermediate I and II; Supplementary Figs. 7, 31) was performed using X-ray diffraction (XRD) and X-ray photoelectron spectroscopy (XPS) (Fig. 3d, e). XRD patterns of intermediate I display attenuated $WO_{2.72}$ reflections and disappearance of selected high-index peaks, indicating pronounced surface amorphization and lattice distortion. In the final $WO_{2.72}/WS_2$ core/shell structure, the WS_2 shell adopts a trigonal 3R phase, whereas reference multilayer WS_2 exhibits the thermodynamically stable hexagonal 2H polymorph. In intermediate II, new diffraction peaks emerge that are absent in both pristine $WO_{2.72}$ and Intermediate I, confirming WS_2 nucleation in agreement with STEM observations. Notably, reflections assignable to both the (013) and (-122) planes of 2H-WS_2 and the (00-9) and (-122) planes of 3R-WS_2 can be identified, indicating the coexistence of transient hexagonal and trigonal stacking in intermediate II. The emergence of a W^{4+} component in intermediate I indicates oxygen-vacancy formation and charge redistribution during reduction. A pronounced increase in W^{4+} intensity in intermediate II confirms substantial WS_2 nucleation at the SGI. Moreover, the lower binding energy of W^{4+} in intermediate II and in the final core–shell structure, compared with 2H-WS_2 references, further supports the formation of 3R-WS_2 on the $WO_{2.72}$ surface. Although these ex-situ results show consistent with phases transitions from $WO_{2.72}$ to hexagonal WS_2 multilayer observed in-situ, the metastable $WO_{2.66}$ phase and trigonal WS_2 during operando studies were not explicitly identified in the intermediates, highlighting the dynamic nature of phase evolution at the SGI reaction and the importance of in-situ techniques.

Integrating in-situ and ex-situ evidence, we propose a WS_2 nucleation mechanism mediated by the dynamically reconstructed SGI (Fig. 3f). (a) Short-range $WO_{2.72\text{-}x}$ structural units and undercoordinated W-O bonds within the amorphous surface layer promote local structural assembly, leading to nucleation of the metastable $WO_{2.66}$ phase. (b) Continued reactions among H_2, sulfur species, and lattice oxygen within crystalline $WO_{2.66}$ domains destabilizes the intermediate, driving its transformation into disordered amorphous cluster. During this stage, the $WO_{2.66}$ nucleus exhibits reversible order–disorder transitions arising from the dynamic competition between short-range structural assembly and dissolution under nonequilibrium conditions. (c) As reduction deepens and sulfur incorporation increases, $WO_{2.66\text{-}x}$ units and reactive W–O species further interact with H_2 and sulfur, triggering the formation of short-range WS_2 structural motifs and culminating in the emergence of a metastable trigonal WS_2 nucleus at the SGI. (d) With continued sulfurization, the metastable trigonal nucleus transforms into the thermodynamically favored hexagonal multilayered phase. These hexagonal multilayered WS_2 nuclei preferentially adopt a vertical orientation on the $WO_{2.72}$ surface, consistent with density functional theory (DFT) calculations (Supplementary Fig. 32), which indicate that vertical alignment is energetically favored over lateral growth.

Atomic reconstruction and nucleation mechanisms at SGI

To model the atomic structural reconstruction of $WO_{2.72}$ nanowire during the SGI reaction, Ab initio molecular dynamics (AIMD) simulations were performed starting from a five-layer $WO_{2.72\text{-}x}$ supercells with graded oxygen-deficiency (W/O ratio gradient: 2.72→2.40→2.40→2.40 →2.30, corresponding to $W_{90}O_{237}$ stoichiometries) (Supplementary Fig. 33). The structural evolution of the five-layer $WO_{2.72\text{-}x}$ atomic system at three stages, 0 ps (initial state), 2.5 ps, and 6.5 ps is shown in Fig. 4a. Compared to the initial lattice and bonding configurations resembling pristine $WO_{2.72}$ crystal (0 ps), structural relaxation induces significant lattice rearrangements, culminating in complete amorphization of the upper most layer (L5) and remarkable distortion of the interlayers (L4-L2) by 2.5 ps. As the structural relaxation continues, more intensified amorphization and distortion can be directly observed by the front and top views of the relaxed structure at 6.5 ps. Furthermore, amorphization and distortion during structural relaxation are quantified by measuring interlayer spacings (vertical distance from each upper-layer W atom to the average height of the layer below) and W-O bond lengths in different lattice layers. The evolution of the parameters, as summarized in Fig. 4b and 4c, reveals that, the broadening of W-O bond length distributions ($\Delta L \geqslant 0.35$ Å) and interlayer spacing fluctuations (e.g., L5-L4 spacing: 2.3-7.3 Å) in amorphous layer are more pronounced than those in distortion layers ($\Delta L \leqslant 0.15$ Å, L4-L3 spacing: 3.0-4.2 Å), indicating greater structural rearrangement and instability in the amorphous region. Moreover, this broadening of interlayer spacings and W-O bond lengths gradually extends from the uppermost layer (L5-L4 spacing: 2.3-7.3 Å, L4-L3 spacing: 3.0-4.2 Å at 2.5 ps) to the interior of the $WO_{2.72}$ crystal (L5-L4 spacing: 2.5-7.3 Å, L4-L3 spacing: 2.4-4.3 Å at 6.5 ps), consistent with the propagation behavior toward the nanowire core.

In addition, the temporal evolution of the coordination number (CN) for a specific W atom in different layers of the five-layer $WO_{2.72-x}$ system provides atomic-level insights into the amorphization and distortion mechanisms. As displayed in Fig. 4d and Supplementary Fig. 34, the CN evolution of a W atom in layer 4 (marked by black circles in Fig. 4a) reveals a hierarchical two-stage mechanism with distinct atomic reorganization behaviors: (1) localized W-O/W-W bond breakage-recombination (0–11.9 ps), followed by (2) stable structural degradation (>11.9 ps). In the early part of the first stage, oxygen vacancy (V_O)-induced charge redistribution and lattice strain not only trigger covalent bond cleavage, evidenced by a rapid CN drop (6 → 5 → 4→ 3) within 0.4 ps, but also accompany the formation of W–W metallic bonding at 0.4 ps. However, this temporary electronic stabilization, along with geometric incompatibility between W–W bonds and the octahedral lattice, accumulates shear strain that eventually exceed the W–W bond energy (≈ 0.47 eV), leading to W–W bond rupture at 0.6 ps and a reversion to the initial stage with renewed W–O cleavage. Moreover, these localized W-O/W-W bond breakage-recombination cycle recurs during the first stage. As structural relax progresses, the fraction of under-coordinated W atoms (CN⩽3) in layers 4-5 increases from 14% to 42% (Supplementary Fig. 35), generating more mobile W atoms that migrate freely and form W-W bonds with the primary W atom at 3.9 ps. Meanwhile, more bonds become geometry-agnostic (bond angles: 69°–144° vs. ideal 90°/180°) and layer identity dissolves (interlayer spacing variance increases by 51%) (Supplementary Tables 2-5). As a result, the initial lattice symmetry collapses, and the formation of diverse W_xO_y polygons impedes coherent realignment, leading to stable amorphous configurations. Compared to the amorphization process, the temporal CN evolution of a specific W atom located in layer 2 (marked by a black rectangle in Fig. 4a), as displayed in Supplementary Fig. 36, only undergo a smaller drop of CN (6 → 5) and localized W-O/W-W bond breakage-recombination. The absence of the collective structural degradation induces distortion of lattice, rather than amorphization.

As sulfur atoms were introduced onto the surface of a relaxed four-layer $WO_{2.72-x}$ system (Supplementary Fig. 37), the resulting $W_{72}O_{184}S_{60}$ hybrid oxide-sulfide structure evokes reactions between S atom and the $WO_{2.72-x}$ lattice, triggering the nucleation of WS_2 within the amorphized surface. AIMD simulations illustrate that S atoms thermodynamically favor reactions with active W-O bonds in the disordered lattice at the uppermost layer of amorphization layer, replacing them with W-S bonds and forming S-W-S units and trigonal prismatic WS_2 nuclei (Fig. 4e and Supplementary Fig. 38). At the atomic level, under-coordinated W atoms (CN$\leqslant$3) in the amorphous matrix serve as preferential adsorption sites for S. Meanwhile, the non-rigid amorphous structure with remarkable bond-angle distortions (71°–162°, Supplementary Table 4), enables topological reorganization to accommodate WS_2 nucleation. Temporal CN evolution for a specific W atom at the top of the amorphous layer (marked by black circles in Fig. 4e), as displayed in Fig. 4f, reveals an atomic substitution-reconstruction nucleation mechanism of W-S bonds on the amorphized $WO_{2.72\text{-}x}$ surface. During the initial nucleation stage (0–3.5 ps), S atoms react with strained W-O bonds, inducing selective sulfur substitution and formation of W-S bond with higher bond strength. After transient W-S bond breaking and reformation, more W-S bonds form, displaying opposite trend of the CN for W-O bonds (3→1) and W-S bonds (1→3). As S ligands connect adjacent W atoms and W-S bonds rotate, adjacent W-S units merge into W_2S_y oligomers (Supplementary Figs. 39-41), enabling trigonal prismatic pre-ordering and nucleation of trigonal WS_2 phase, corroborating the operando observations.

The observed lattice reconstruction and subsequent dual-layer-mediated nucleation are not unique to the S-$WO_{2.72}$ system. Comparable SGI-induced lattice reconstruction and dual-layer-mediated nucleation behaviors are also observed in the S-MoO_2 system, where pronounced surface lattice decomposition, subsurface distortion, and subsequent nucleation of layered MoS_2 are directly resolved at the atomic scale (Supplementary Fig. 42). The emergence of an amorphous–distorted interphase prior to sulfide formation suggests that dual-layer reconstruction represents a general kinetic intermediate in transition-metal oxide–chalcogen SGI reactions. Beyond tungsten and molybdenum oxides, ex-situ investigations of SGI reactions on ZnO nanowires (Supplementary Figs. 43-45) and Au nanoparticles (Supplementary Fig. 46) reveal similar surface lattice destabilization and interfacial restructuring preceding phase transformation. Despite differences in bonding character and crystal symmetry, these systems consistently exhibit transient amorphization, subsurface distortion, and defect-mediated nucleation, underscoring the universality of dual-layer formation under nonequilibrium solid–gas conditions (Supplementary Note 4). Thus, these findings establish dynamically reconstructed dual-layer interfaces as general mechanistic motif governing SGI reactions. Rather than proceeding through a simple reaction-front propagation, SGI conversion involves adaptive interfacial restructuring that regulates defect generation, mass transport, and nucleation pathways. This generalized mechanism provides a unified framework for understanding chalcogenization, reduction, and heterogeneous phase transformation processes across diverse solid–gas systems.

Using an environmental transmission electron microscopy cell as a microreaction chamber for real-time imaging, we achieved atomic-scale, real-time monitoring of solid-gas interface reaction at low temperatures (≈ 200-300 °C) on the surface of oxygen-deficient transition metal oxide nanowires ($WO_{2.72}$, $MoO_{2.75}$). Our observations reveal that initial SGI reactions induce surface restructuring into a dual-layer configuration: an amorphous surface layer and a subsurface distorted lattice layer. These layers act synergistically to govern SGI reactions, overturning conventional models that assume a simple reaction front separating a pristine core from a uniform product layer. The dual-layer configuration plays key roles in SGI reactions: the amorphous layer serves as a dynamic precursor reservoir, facilitating short-range ordering and critical nucleus formation through reversible crystalline–amorphous transitions, while the subsurface rough interface, characterized by atomic steps, vacancies, and lattice mismatch, provides energetically favorable sites for nucleation and growth (e.g., vertical WS_2 growth). Notably, our real-time observations capture the phase transition from $WO_{2.72}$ to 2H-WS_2, highlighting the role of metastable orthorhombic $WO_{2.66}$ and trigonal WS_2 phases in facilitating nucleation and phase transition. These findings fundamentally challenge static reaction front models and establish a dual-layer-mediated reconstruction and nucleation paradigm for SGI reactions. They also provide direct experimental evidence of the multistep nucleation mechanism of WS_2 during SGI CVD, offering new insights into previously inaccessible mechanistic phenomena and laying the foundation for effectively controlling diverse SGI processes.

Methods

Preparation of transition metal oxidate nanowires

The synthesis was adapted from established chemical vapor deposition approaches (as reported in ref.[35]), with modifications to control precursor delivery and reaction kinetics. $WO_{2.72}$ nanowires were grown in a one-zone tube furnace using WO_3 (MoO_3) powder (99.99%, Alfa Aesar) as the oxide source and sulfur (99.999%, Alfa Aesar) as the chalcogen precursor. The oxide precursor was positioned at the center of the heating zone, while sulfur was placed upstream (≈ 40 cm) to decouple its evaporation from that of the oxide. Silicon substrates coated with an ≈10 nm Au film (deposited by radio-frequency magnetron sputtering and annealed at 750 °C for 10 min to form catalyst nanoparticles) were placed downstream (≈ 30 cm) to enable subsequent nucleation and growth. The reaction was conducted under reduced pressure (850–950 mbar) with controlled gas flow. Prior to growth, the system was purged with high-purity argon (1,215 cm^3 STP min^{-1}, 5 min). Upon heating, the oxide precursor was vaporized and transported to the catalyst sites, while hydrogen was introduced at intermediate temperature (800 °C for WO_3, 550 °C for MoO_3) to regulate the chemical environment. The system was then brought to the growth temperature (900 °C for WO_3, 630 °C for MoO_3), at which point sulfur evaporation was initiated via rapid translation of the precursor into the heating zone, enabling synchronized supply of reactants. Growth proceeded under argon flow (150 cm^3 STP min^{-1}), followed by post-growth purging (500 cm^3 STP min^{-1}) during natural cooling. This protocol yields oxygen-deficient transition metal oxide nanowires with controlled morphology and composition.

Transformation of transition metal oxidate nanowires

The synthesized $WO_{2.72}$ (MoO_2) crystals are redispersed and uniformly dispersed in the ethanol by ultrasonic treatment for further processing. Then, ethanolic $WO_{2.72}$ crystals are dispersed onto the Si_3N_4 electron-transparent window. The membrane side of the atmosphere E-chips was plasma cleaned for 3 min to increase the hydrophilicity of the E-chip surface. This contributes to a more $WO_{2.72}$ crystal sample distribution. To prevent the carbon deposition on the surface of pre-synthesized $WO_{2.72}$ crystals and enable atomic-resolution imaging, we increase the temperature of sample to 200 ºC and keep it for 2 min before the in-situ imaging.

In-situ and ex-situ characterization

The atomic-scale in-situ observations were performed by transmission electron microscopy (JEM-2100 microscope) equipped with an atmosphere TEM holder (Protochips Inc.). The microscope was operated at an accelerating voltage of 200 kV. Imaging was performed primarily in TEM mode with a probe current of 1.1 nA, corresponding to an estimated current density at the specimen of 10^{-2} A cm^{-2}. For time-resolved imaging, the electron dose rate was approximately 7×10^4 e^- nm^{-2} s^{-1}. Low-dose conditions were used whenever possible, and beam blanking was applied between acquisitions to minimize unintended irradiation effects. The atmosphere holder contains the E-chips, provides a gas and electrical path to the E-chips, and hermetically seals the closed cell in the TEM. The sample is contained between a pair of E-chips, both with electron transparent windows, within the holder tip. The gas management system enables the gas flow and gas pressure control inside the holder. It is also used to prepare gas mixtures prior to the experiment. The pneumatic valves control the entry and exhaust of experiment and purge gases and are used to fill either of two experiment tanks for storing and delivering of these gases. The vacuum tank provides a pressure differential to control and set pressure in the experiment tanks and holder. The manifold has a pressure relief valve set to 22 psig (1.5 bar) to protect the system if it becomes over-pressurized, which would result in a gas experiment error. A roughing (scroll) pump removes gases from the manifold and the holder when in operation. All subsystems are controlled with a Windows-based desktop computer using the Atmosphere Clarity software through the electronics control unit (ECU). The atmosphere in the TEM cell is operated using a custom workflow-based software package called Clarity, which features a powerful yet easy-to-use interface and flexible design. It provides at-a-glance information so the TEM operator can quickly see the current system status yet maintain focus on the TEM and experiment. During the in-situ experiment, the environmental cell was supplied with mixed-gas of 10% H_2 and 90% Ar with a purity of 99.99% (H_2) and 99.9% (Ar). And S vapor is provided by evaporating S powder during the increasement of temperature. The total pressure during experiments was 700 Torr, measured at the cell inlet. Before the increasement of temperature in the cell, three pump/purge cycles were carried to displace and remove residual gases in the cell. When the solid-gas reaction starts, the exhaust valve remains closed and the intake valve stays open for the duration of the experiment to maintain stable pressure and a continuous hydrogen supply.

A ceramic heating membrane ensures precious temperature control in the TEM cell. Atmosphere software to ensure accurate and precise temperature control. The closed loop temperature control uses the calibration file when actively adjusting the temperature in different gas environments and is based on the resistance of the SiC membrane. To maximize electron transparency in the TEM, an array of 6 holes, ≈ 9 μm in diameter, are patterned in each membrane. The heating area is limited to this array of holes and is approximately 90 μm in area. The investigated nanowires typically spanned 2–3 μm and were positioned over the hole region, corresponding to the central area of most uniform temperature. Therefore, any axial temperature gradient along an individual nanowire can be considered negligible under the present in-situ experimental conditions. In other words, the spatial temperature distribution across the region of interest is effectively uniform, taking into account the membrane's thermal conductivity, nanowire geometry, and gas convection effects.

The ex-situ HAADF-STEM characterization was conducted using a Double Cs Corrector transmission electron microscope operated at an accelerating voltage of 300 kV. The microscope is equipped with probe- and image-side spherical aberration correctors to enable high-resolution imaging, and an integrated energy-dispersive X-ray spectroscopy (EDS) detector for compositional analysis. This system achieves an information resolution of 70 pm and a scanning TEM (STEM) spatial resolution of 50 pm, allowing direct visualization of atomic-scale structures. Ex-situ structural analysis of crystal phase and binding energy of elements were performed using Bruker X-ray diffractometer (D8 DISCOVER A25) and X-ray Photoelectron Spectrometer (Axis Supra).

DFT calculations and theoretical analysis

The density functional theory (DFT) calculations were performed using the VASP package[36]. The exchange-correlation potential and ion-electron interactions were described using the generalized gradient approximation (GGA) and projected augmented wave (PAW) method[37, 38]. A plane-wave basis energy cutoff of 500 eV was used. The van der Waals interactions were addressed by the semi-empirical DFT-D2 method[39, 40]. A 1×1×1 Monkhorst-Pack k-point mesh was adopted. The formation energies of 1D WS_2-substrate hybrid interface, namely,

$$E_{\mathrm{f}} = (E_{\mathrm{WS_2}} + E_{\mathrm{sub}} - E_{\mathrm{hyb}})/A, \qquad (1)$$

where E_{hyb} is the total energy of the hybrid; E_{WS2} and E_{sub} denote the total energies of 1D WS_2 and substrates, respectively; and A is the area of bilayer interface. The positive formation energy can represent the interface stability, and the larger the positive value, the more stable it is. To study the evolution process of tungsten atoms binding with $WO_{2.72}$ crystal, the potential energy surface was search using the climbing-image nudged elastic band (CINEB) method[41, 42].

We computed lattice reconstruction of $WO_{2.72}$ nanowire during SGI reaction through DTT calculations using projector augmented-wave (PAW) method and the Perdew-Burke-Ernzer-hof (PBE) exchange–correlation functional. All calculations were performed in the canonical (*NVT*) ensemble at 1700 K, with temperature control effected by an Nose-Hoover thermostat[43] coupled to the velocity Verlet integrator. A time step of 1.5 fs was used. Lattice parameters were held fixed while only atomic positions were allowed to relax. To reduce computational cost, a plane-wave cutoff energy of 300 eV and a 1×1×1 Monkhorst–Pack k-point mesh was adopted. A 10 Å vacuum slab was introduced along the [001] direction to suppress image–image interactions, and the bottommost atomic layer was constrained to eliminate spurious boundary effects. Starting from the pristine $WO_{2.72}$ ($W_{18}O_{49}$) crystal ($\alpha = 90°$, $\beta = 90°$, $\gamma = 110°$; $a = 18.287$ Å, $b = 14.199$ Å, $c = 3.859$ Å), multilayer supercells with graded oxygen-vacancy distributions were constructed. Four-layer (1×1×4) and five-layer (1×1×5) models—corresponding to $W_{72}O_{184}$ and $W_{90}O_{237}$ stoichiometries, respectively—were generated along [001]. In the four-layer supercell, the W/O ratio decreased from 2.72 at the bottom to 2.30 at the surface (2.72→2.60→2.60→2.30). In the five-layer system, it followed a gradient of 2.72→2.40→2.40→2.40→2.30. Subsequent to full structural relaxation of the four-layer model, surface sulfurization was performed by introducing 60 sulfur atoms, yielding a $W_{72}O_{184}S_{60}$ hybrid oxide-sulfide system for investigation of the effects of sulfide modification on surface properties.

Data availability

The data that support the findings of this study are available from the corresponding authors upon request. Thermodynamic data used in this study are available from the Open Quantum Materials Database (https://oqmd.org/analysis/phase_diagram/). Source data are provided with this paper.

References

1. King, P.L. et al. Gas–Solid Reactions: Theory, Experiments and Case Studies Relevant to Earth and Planetary Processes. *Reviews in Mineralogy and Geochemistry* **84**, 1-56 (2018).

2. Fedunik-Hofman, L., Bayon, A. & Donne, S.W. Kinetics of Solid-Gas Reactions and Their Application to Carbonate Looping Systems. *Energies* **12**, 2981 (2019).
3. Cao, L. et al. Atomically dispersed iron hydroxide anchored on Pt for preferential oxidation of CO in H(2). *Nature* **565**, 631-635 (2019).
4. Yuan, W. et al. Visualizing H(2)O molecules reacting at TiO(2) active sites with transmission electron microscopy. *Science* **367**, 428-430 (2020).
5. Muravev, V. et al. Interface dynamics of Pd–CeO2 single-atom catalysts during CO oxidation. *Nature Catalysis* **4**, 469-478 (2021).
6. Sankar, M. et al. Role of the Support in Gold-Containing Nanoparticles as Heterogeneous Catalysts. *Chem Rev* **120**, 3890-3938 (2020).
7. Stamenkovic, V.R. et al. Improved oxygen reduction activity on Pt3Ni(111) via increased surface site availability. *Science* **315**, 493-497 (2007).
8. Bruce, P.G., Freunberger, S.A., Hardwick, L.J. & Tarascon, J.M. Li-O2 and Li-S batteries with high energy storage. *Nat Mater* **11**, 19-29 (2011).
9. Miller, D.R., Akbar, S.A. & Morris, P.A. Nanoscale metal oxide-based heterojunctions for gas sensing: A review. *Sensors and Actuators B: Chemical* **204**, 250-272 (2014).
10. Khan, M.A.H., Rao, M.V. & Li, Q. Recent Advances in Electrochemical Sensors for Detecting Toxic Gases: NO(2), SO(2) and H(2)S. *Sensors (Basel)* **19** (2019).
11. Li, G. et al. Review of micro-arc oxidation of titanium alloys: Mechanism, properties and applications. *Journal of Alloys and Compounds* **948**, 169773 (2023).
12. Gao, D. et al. Review of progress in calculation and simulation of high-temperature oxidation. *Progress in Materials Science* **147**, 101348 (2025).
13. Sun, L. et al. Chemical vapour deposition. *Nature Reviews Methods Primers* **1** (2021).
14. Shi, Y., Li, H. & Li, L.J. Recent advances in controlled synthesis of two-dimensional transition metal dichalcogenides via vapour deposition techniques. *Chem Soc Rev* **44**, 2744-2756 (2015).
15. Cai, Z., Liu, B., Zou, X. & Cheng, H.M. Chemical Vapor Deposition Growth and Applications of Two-Dimensional Materials and Their Heterostructures. *Chem Rev* **118**, 6091-6133 (2018).
16. Chen, P. et al. Engineering solvation in initiated chemical vapour deposition for control over polymerization kinetics and material properties. *Nature Synthesis* (2023).
17. Jiao, L. et al. Chemical vapour deposition of Fe-N-C oxygen reduction catalysts with full utilization of dense Fe-N(4) sites. *Nat Mater* **20**, 1385-1391 (2021).
18. Luo, J. et al. Vapour-deposited perovskite light-emitting diodes. *Nature Reviews Materials* **9**, 282-294 (2024).
19. Vinu, R. Gas–Solid Reactions and Reactors. 161-271 (2017).
20. Ramachandran, P.A. & Doraiswamy, L.K. Modeling of noncatalytic gas-solid reactions. *AIChE Journal* **28**, 881-900 (1982).
21. Wang, J. Continuum theory for dense gas-solid flow: A state-of-the-art review. *Chemical Engineering Science* **215**, 115428 (2020).
22. Frey, H., Beck, A., Huang, X., van Bokhoven, J.A. & Willinger, M.G. Dynamic interplay between metal nanoparticles and oxide support under redox conditions. *Science* **376**, 982-987 (2022).
23. Monai, M. et al. Restructuring of titanium oxide overlayers over nickel nanoparticles during catalysis. *Science* **380**, 644-651 (2023).

24. Yuan, W. et al. In situ manipulation of the active Au-TiO(2) interface with atomic precision during CO oxidation. *Science* **371**, 517-521 (2021).
25. Chen, X. et al. Atomic dynamics of gas-dependent oxide reducibility. *Nature* **644**, 927-932 (2025).
26. Tenne, R., Margulis, L., Genut, M. & Hodes, G. Polyhedral and cylindrical structures of tungsten disulphide. *Nature* **360**, 444-446 (1992).
27. Zak, A. et al. Scaling Up of the WS2Nanotubes Synthesis. *Fullerenes, Nanotubes and Carbon Nanostructures* **19**, 18-26 (2010).
28. Liu, Z. et al. WS2 Nanotubes, 2D Nanomeshes, and 2D In-Plane Films through One Single Chemical Vapor Deposition Route. *ACS Nano* **13**, 3896-3909 (2019).
29. Chithaiah, P. et al. Solving the "MoS(2) Nanotubes" Synthetic Enigma and Elucidating the Route for Their Catalyst-Free and Scalable Production. *ACS Nano* **14**, 3004-3016 (2020).
30. Luo, L. et al. Symmetry-broken MoS(2) nanotubes through sequential sulfurization of MoO(2) nanowires. *Nat Commun* **16**, 8394 (2025).
31. Kundrat, V. et al. Mechanism of WS(2) Nanotube Formation Revealed by in Situ/ex Situ Imaging. *ACS Nano* **18**, 12284-12294 (2024).
32. Zhang, Q. et al. Atomic dynamics of electrified solid-liquid interfaces in liquid-cell TEM. *Nature* **630**, 643-647 (2024).
33. Lee, Y.-J., Lee, T. & Soon, A. Phase Stability Diagrams of Group 6 Magnéli Oxides and Their Implications for Photon-Assisted Applications. *Chemistry of Materials* **31**, 4282-4290 (2019).
34. Jeon, S. et al. Reversible disorder-order transitions in atomic crystal nucleation. *Science* **371**, 498-503 (2021).
35. An, Q. et al. Direct growth of single-chiral-angle tungsten disulfide nanotubes using gold nanoparticle catalysts. *Nat Mater* **23**, 347-355 (2024).
36. Kresse, G. & Furthmuller, J. Efficiency of ab-initio total energy calculations for metals and semiconductors using a plane-wave basis set. *Computational Materials Science* **6**, 15-50 (1996).
37. Blochl, P.E. PROJECTOR AUGMENTED-WAVE METHOD. *Physical Review B* **50**, 17953-17979 (1994).
38. Perdew, J.P., Burke, K. & Ernzerhof, M. Generalized gradient approximation made simple (vol 77, pg 3865, 1996). *Physical Review Letters* **78**, 1396-1396 (1997).
39. Kerber, T., Sierka, M. & Sauer, J. Application of semiempirical long-range dispersion corrections to periodic systems in density functional theory. *Journal of Computational Chemistry* **29**, 2088-2097 (2008).
40. Grimme, S. Semiempirical GGA-type density functional constructed with a long-range dispersion correction. *Journal of Computational Chemistry* **27**, 1787-1799 (2006).
41. Sheppard, D., Terrell, R. & Henkelman, G. Optimization methods for finding minimum energy paths. *Journal of Chemical Physics* **128** (2008).
42. Sheppard, D., Xiao, P., Chemelewski, W., Johnson, D.D. & Henkelman, G. A generalized solid-state nudged elastic band method. *Journal of Chemical Physics* **136** (2012).
43. Hoover, W.G. Canonical dynamics: Equilibrium phase-space distributions. *Phys Rev A Gen Phys* **31**, 1695-1697 (1985).

Acknowledgements

Q.A. thanks the Analytical & Testing Center of Northwestern Polytechnical University for SEM, TEM, STEM, and ETEM measurements.

Funding

S.Y. discloses support for the research of this work from the National Natural Science Foundation of China [12425407] and the Major Program of Hubei Province [2023BAA020]. Q.A. discloses support for the research of this work from the Fundamental Research Funds for the Central Universities [G2025KY06140]. W.Z. discloses support for the research of this work from the National Natural Science Foundation of China [12104513].

Author contributions:

Q.A. conceived the original idea for the project. Q.A. and X. Z. prepared the samples, Q.A. performed SEM, TEM, STEM, XRD and XPS characterizations and analyzed all the experimental data. Q.A. carried out the operando study on the WS_2 and MoS_2 nucleation and growth using environmental transmission electron microscope. J.W. and X. Z. provide assistance in performing the operando experiments. Y. F. and W.Z. carried out the calculations for lattice reconstruction and nucleation at SGI. W. X. and S.Y. performed first-principles calculations for vertical growth of WS_2 on $WO_{2.72}$. X.Z. and F. L. provide assistance in preparing and transforming samples for the operando study. Q.A. wrote the paper. Q.A. and W.Z. revised the paper. All authors commented on the manuscript.

Competing interests

The authors declare no competing interests.

Fig. 1 | Design concept and atomic solid-gas interface reaction paradigm. a, Schematic of environmental TEM reaction cell, integrated a heating holder. **b, c,** Pristine $WO_{2.72}$ nanowire surface prior to reaction with S vapor and H_2. Atomic model of lattice on the surface of nanowire is displayed. Insets display the corresponding FFT patterns. Scale bar, 2 nm^{-1}. **d,** Pristine $WO_{2.72}$ nanowire surface after a short-time annealing, effectively removing carbon deposition induced by in-situ TEM imaging. **e,** Operando strategy used in this study uncover dynamic reaction pathway at solid-gas interfaces: initial gas adsorption and reactions trigger surface rearrangement and defects formation, structural restructuring induces a dual-layer configuration: an uppermost amorphous phase (a quasi-liquid interphase) and a subsurface lattice-distorted and condensed region, mediating nucleation of $WO_{2.66}$ nuclei and growth of multilayer WS_2. **g-j,** In-situ TEM frames of corresponding resulting SGI structures. The resulting SGI is indicated by white dotted lines in (**g**); the interfaces between amorphous, distorted and pristine layers are indicated by dotted lines, and the arrow shows the progression orientation in (**h**); nucleation of $WO_{2.72}$ nucleus (**g**) and vertical growth of multilayer WS_2 (**j**) mediated by the dual-layer reconstruction. The atomic reconstruction and nucleation dynamics shown in panels **g-j** represent a general and consistent phenomenon. These observations have been independently confirmed by at least five different regions of the SGI, all showing similar behavior.

Fig. 2 | Atomic-scale dynamics of dual-layer formation during solid-gas reactions. a, In-situ TEM frame of SGIs at 3 min 4s, revealing typical dual-layer structure consisting of amorphous layer, distorted interlayer and pristine lattice, which is marked by blue and yellow dotted lines, respectively. Insets show the corresponding FFT pattern from the region indicated by blue and orange rectangle. **b,** Zoom-in TEM frame of the region marked by white rectangle in a, displaying dynamic behavior of atomic rearrangement. The corresponding atomic models of the lattice in this region are displayed. The atomic reconstruction dynamics shown in panels a, b represent a general and consistent phenomenon. These observations have been independently confirmed at least five different regions of the SGI, all showing similar behavior. **c,** Schematic of atomic rearrangement and bond reorganization at evolving SGIs. **d,** Time-resolved in-situ TEM frame of SGIs, revealing progressive dynamics of the dual-layer structure at SGI interface, with insets showing FFT patterns from the regions marked by blue and orange rectangle, which corresponds to the surface and interior region of the $WO_{2.72}$ crystal, respectively. The blue and orange line indicated the interface between amorphous and distorted layer and distorted and pristine layer, respectively. **e, f,** Interlayer spacings-evolution of pristine interior and distorted surface regions (e) and thickness-evolution of the distorted layer (f) from in-situ TEM observation showing the structural dynamics during the SGI reactions. The error bars represent the mean ± standard deviation from four independent regions at SGI. Source data are provided as a Source Data file.

Fig. 3 | Atomic dynamic of nucleation and phase transition during subsequent SGI reactions. a, b, Time-resolved in-situ TEM images showing nucleation and structural dynamics of two distinct crystalline phases at the SGI. Scale bar, 2 nm. Insets show corresponding FFT patterns. **c,** Energy landscape of the ternary W-S-O system, highlighting polymorphic orthorhombic $WO_{2.66}$ (red star) and phases-separating trigonal WS_2 (brown star) metastable phases. The energy landscape of the ternary W-S-O system and phase stability diagram was constructed using formation energies obtained from the Open Quantum Materials Database (OQMD). **d, e,** Comparative XRD patterns and XPS spectra of the pristine $WO_{2.72}$ nanowire, intermediate phases, and multilayer WS_2. **f,** Schematic illustration of the nucleation and phase-transition dynamics during the progression of the SGI reaction. Source data are provided as a Source Data file.

Fig. 4 | Proposed mechanism of lattice reconstruction and WS_2 nucleation at SGI. a, Snapshots of front and top views of initial, intermediate (2.5 ps) and final structure (6.5 ps). The initial structure model represents the resulting $WO_{2.72-x}$ structure after reaction with H and S atom. Two typical W atoms in layer 4 and layer 2 are marked by a circle and a triangle, respectively. **b, c,** Comparison of the interlayer spacings (b) and W-O bond lengths (c) in different layers during the structural evolution. **d,** Temporal evolution of the coordination number (CN) for W-O bonds of a specific W atom located in layer 4 (marked by a black circle in panel a). W-O bond configurations at specific selected time points are shown. **e,** Snapshot of initial and intermediate structure (7.5 ps) with 60 sulfur atoms introduced onto the surface of a relaxed four-layer $WO_{2.72-x}$ atomic system, yielding a $W_{72}O_{184}S_{60}$ hybrid oxide-sulfide structure. **f,** Temporal evolution of the CN for W-O and W-S bonds of a specific W atom located in uppermost layer of a relaxed four-layer $WO_{2.72-x}$ atomic system (marked by a black triangle in e). W-O/ and W-S bonds configurations at specific selected time points are shown. Source data are provided as a Source Data file.

The dynamics at solid-gas interfaces at the atomic level remain a challenge due to transient processes and complex interfacial conditions. Here, the authors directly visualize reactions at the solid-gas interface and demonstrate a double-layer reconstruction that controls the nucleation and vertical growth of WS_2 on $WO_{2.72}$ nanowires.

Peer Review Information: *Nature Communications* thanks Won Chul Lee, and the other, anonymous, reviewer for their contribution to the peer review of this work. A peer review file is available.

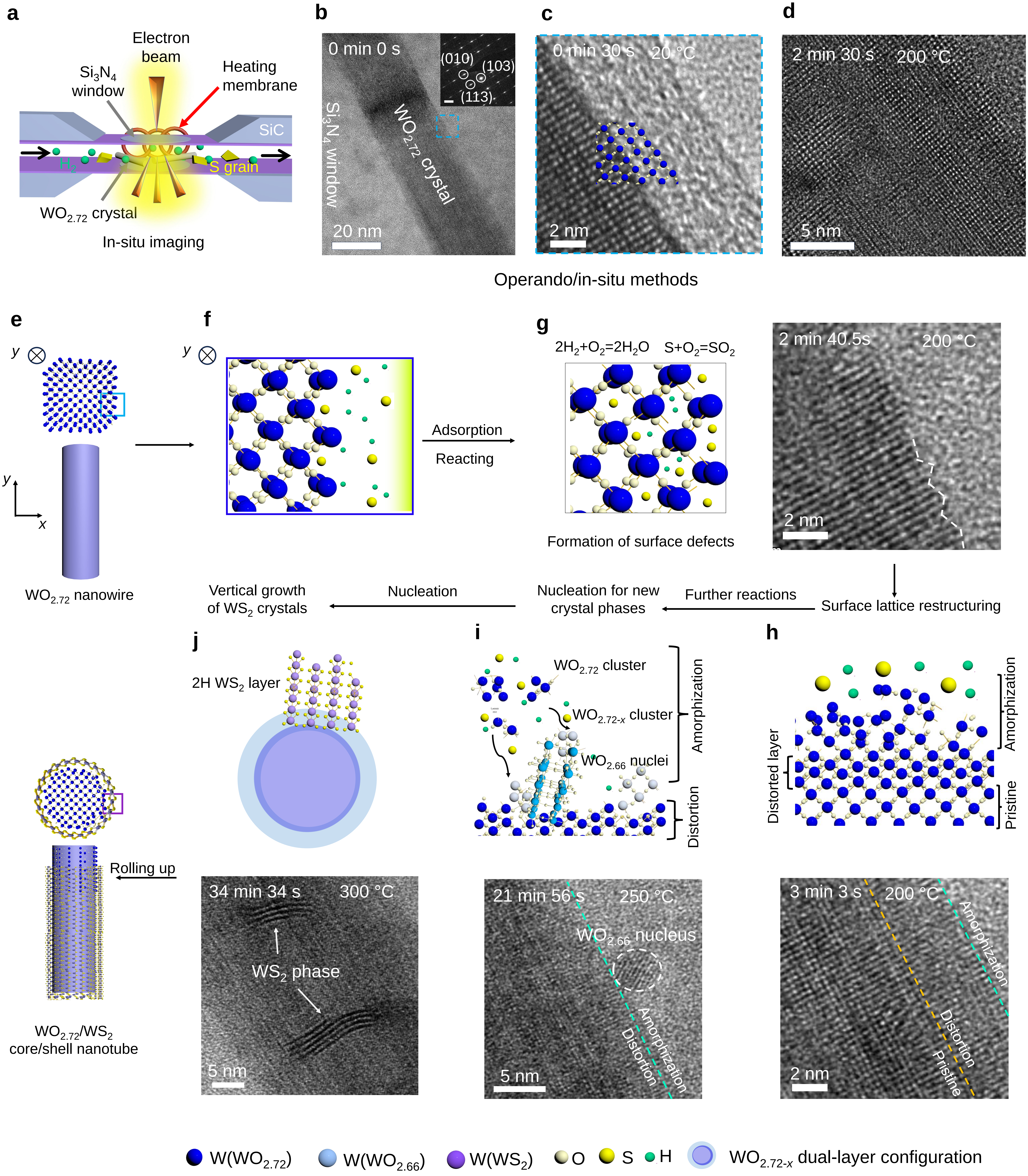
a
Electron beam
Si_3N_4 window
Heating membrane
SiC
H_2
S grain
$WO_{2.72}$ crystal
In-situ imaging
b
0 min 0 s
(010)
(103)
(113)
Si_3N_4 window
$WO_{2.72}$ crystal
20 nm
c
0 min 30 s
20 °C
2 nm
d
2 min 30 s
200 °C
5 nm
Operando/in-situ methods
e
y
y
x
$WO_{2.72}$ nanowire
f
y
Adsorption
Reacting
g
$2H_2+O_2=2H_2O$
$S+O_2=SO_2$
Formation of surface defects
2 min 40.5s
200 °C
2 nm
Surface lattice restructuring
Further reactions
Nucleation for new crystal phases
Nucleation
Vertical growth of WS_2 crystals
j
2H WS_2 layer
i
$WO_{2.72}$ cluster
$WO_{2.72-x}$ cluster
$WO_{2.66}$ nuclei
Amorphization
Distortion
h
Distorted layer
Amorphization
Pristine
Rolling up
$WO_{2.72}/WS_2$ core/shell nanotube
34 min 34 s
300 °C
WS_2 phase
5 nm
21 min 56 s
250 °C
$WO_{2.66}$ nucleus
Amorphization
Distortion
5 nm
3 min 3 s
200 °C
Amorphization
Distortion
Pristine
2 nm
$W(WO_{2.72})$
$W(WO_{2.66})$
$W(WS_2)$
O
S
H
$WO_{2.72-x}$ dual-layer configuration

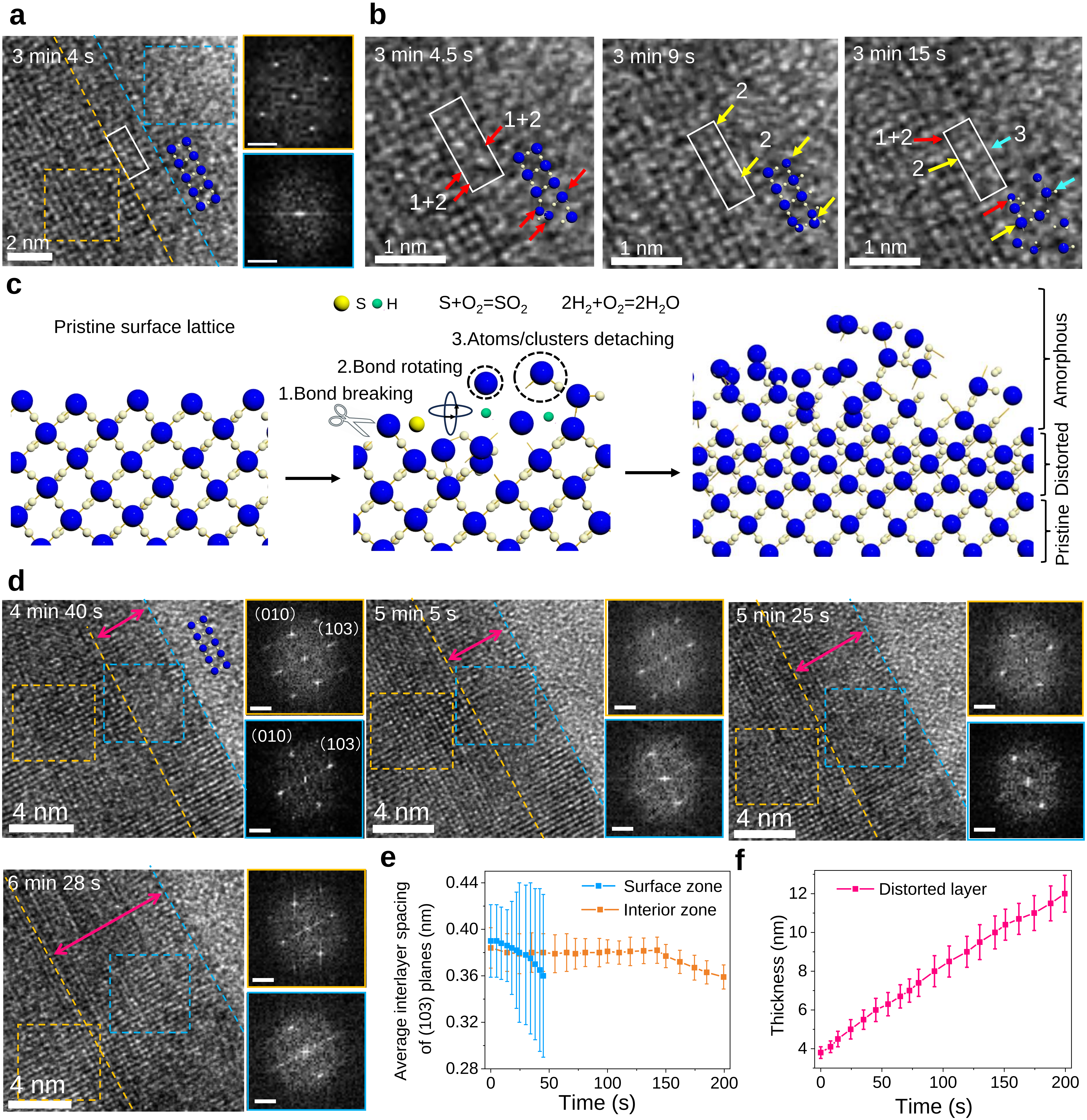
a
3 min 4 s
2 nm
b
3 min 4.5 s
1+2
1+2
1 nm
3 min 9 s
2
2
1 nm
3 min 15 s
1+2
2
3
1 nm
c
Pristine surface lattice
S H
$S+O_2=SO_2$
$2H_2+O_2=2H_2O$
3.Atoms/clusters detaching
2.Bond rotating
1.Bond breaking
Amorphous
Distorted
Pristine
d
4 min 40 s
(010)
(103)
(010)
(103)
4 nm
5 min 5 s
4 nm
5 min 25 s
4 nm
6 min 28 s
4 nm
e
Surface zone
Interior zone
Average interlayer spacing of (103) planes (nm)
0.44
0.40
0.36
0.32
0.28
0
50
100
150
200
Time (s)
f
Distorted layer
Thickness (nm)
12
10
8
6
4
0
50
100
150
200
Time (s)


a
Nucleation
(010)
3 min 52 s
Ordered $WO_{2.66}$ nuclei
3 min 54 s
$WO_{2.66}$ crystallite
3 min 56 s
(010)
(103)
(001)
4 min 0 s
0.383 nm
0.375 nm
b
Nucleation
21 min 17 s
Trigonal WS_2 nuclei
21 min 27 s
(012)
0.268 nm
Growth
22 min 38 s
Vertical 2H WS_2 layer
22 min 41 s
(005)
0.622 nm
c
0.0
−0.5
−1.0
−1.5
−2.0
Formation energy (eV)
O
SO_3
WS_2O_9
WO_3
$WO_{2.72}$
SO_2
$WO_{2.66}$
S_8O
S
$1T\text{-}WS_2/WS_2$
W
d
Intensity
2D WS_2 multilayers
(002)
(013)
(015)
(-122)
(022)
(-124)
(00-3)
(-114)
$WO_{2.72}/WS_2$ core-shell nanowire
(00-9)
(00-6)
(012)
(018)
(-120)
(013)
(00-9)
I- II
(018)
(-122)
I- I
$WO_{2.72}$ nanowire
(004)
(104)
(012)
(-605)
(600)
(103)
(-503)
(-121)
(321)
(225)
10
20
30
40
50
60
70
2Θ (degree)
e
$WO_{2.72}$ nanowire
Intensity
I- I
44
40
36
32
Binding energy (eV)
Intensity
I- I
I- II
$WO_{2.72}/WS_2$ nanowire
2D WS_2 layer
44
40
36
32
Binding energy (eV)
f
Free W-O bonding
Short-range $WO_{2.72\text{-}x}$ units
Short-range $WO_{2.66\text{-}x}$ units
S
H
Amorphous layer
Ordered $WO_{2.66}$ nuclei
1 Nucleation
Disorder
2 Disordering
3 Amorphization
4 Nucleation
Trigonal WS_2 nuclei
5 Growth
Vertical 2H WS_2 layer
Distortion layer
$WO_{2.72}$ nanowire

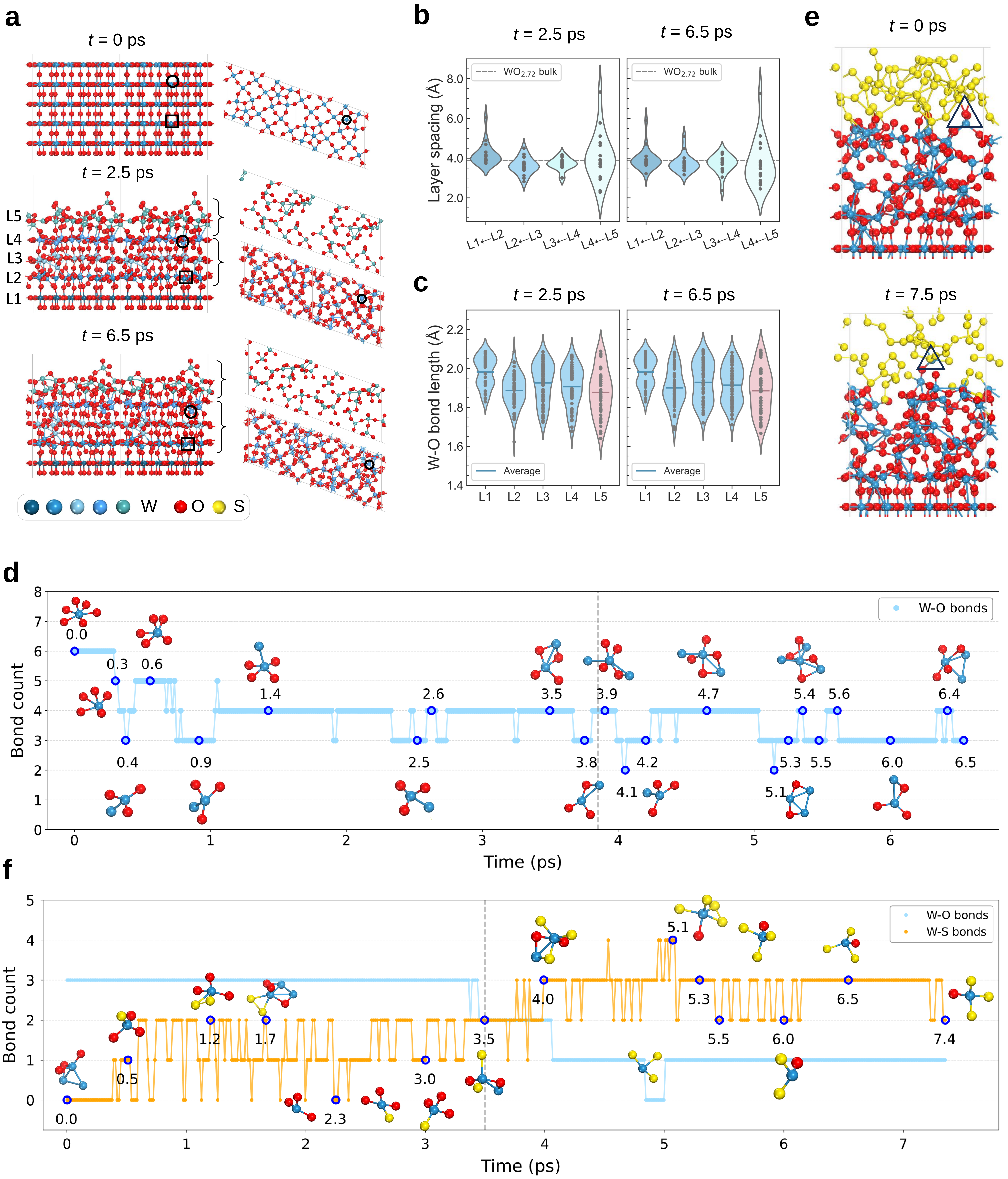
a
t = 0 ps
t = 2.5 ps
t = 6.5 ps
L5
L4
L3
L2
L1
W
O
S
b
t = 2.5 ps
t = 6.5 ps
WO$_{2.72}$ bulk
Layer spacing (Å)
8.0
6.0
4.0
2.0
L1←L2
L2←L3
L3←L4
L4←L5
c
t = 2.5 ps
t = 6.5 ps
W-O bond length (Å)
2.2
2.0
1.8
1.6
1.4
Average
L1
L2
L3
L4
L5
e
t = 0 ps
t = 7.5 ps
d
W-O bonds
Bond count
Time (ps)
0.0
0.3
0.6
1.4
2.6
3.5
3.9
4.7
5.4
5.6
6.4
0.4
0.9
2.5
3.8
4.1
4.2
5.1
5.3
5.5
6.0
6.5
f
W-O bonds
W-S bonds
Bond count
Time (ps)
0.0
0.5
1.2
1.7
2.3
3.0
3.5
4.0
5.1
5.3
5.5
6.0
6.5
7.4